Front. Earth Sci. 2019, 13(3): 478–494
https://doi.org/10.1007/s11707-018-0702-5

RESEARCH ARTICLE

Automatic sub-pixel coastline extraction based on spectral mixture analysis using EO-1 Hyperion data

Zhonghua HONG (✉)[1,2], Xuesu LI[1], Yanling HAN (✉)[1], Yun ZHANG[1], Jing WANG[1], Ruyan ZHOU[1], Kening HU[1]

1 College of Information Technology, Shanghai Ocean University, Shanghai 201306, China
2 Key Laboratory of Fisheries Information, Ministry of Agriculture, Shanghai 201306, China

Abstract Many megacities (such as Shanghai) are located in coastal areas, therefore, coastline monitoring is critical for urban security and urban development sustainability. A shoreline is defined as the intersection between coastal land and a water surface and features seawater edge movements as tides rise and fall. Remote sensing techniques have increasingly been used for coastline extraction; however, traditional hard classification methods are performed only at the pixel-level and extracting sub-pixel accuracy using soft classification methods is both challenging and time consuming due to the complex features in coastal regions. This paper presents an automatic sub-pixel coastline extraction method (ASPCE) from high-spectral satellite imaging that performs coastline extraction based on spectral mixture analysis and, thus, achieves higher accuracy. The ASPCE method consists of three main components: 1) A Water-Vegetation-Impervious-Soil (W-V-I-S) model is first presented to detect mixed W-V-I-S pixels and determine the endmember spectra in coastal regions; 2) The linear spectral mixture unmixing technique based on Fully Constrained Least Squares (FCLS) is applied to the mixed W-V-I-S pixels to estimate seawater abundance; and 3) The spatial attraction model is used to extract the coastline. We tested this new method using EO-1 images from three coastal regions in China: the South China Sea, the East China Sea, and the Bohai Sea. The results showed that the method is accurate and robust. Root mean square error (RMSE) was utilized to evaluate the accuracy by calculating the distance differences between the extracted coastline and the digitized coastline. The classifier's performance was compared with that of the Multiple Endmember Spectral Mixture Analysis (MESMA), Mixture Tuned Matched Filtering (MTMF), Sequential Maximum Angle Convex Cone (SMACC), Constrained Energy Minimization (CEM), and one classical Normalized Difference Water Index (NDWI). The results from the three test sites indicated that the proposed ASPCE method extracted coastlines more efficiently than did the compared methods, and its coastline extraction accuracy corresponded closely to the digitized coastline, with 0.39 pixels, 0.40 pixels, and 0.35 pixels in the three test regions, showing that the ASPCE method achieves an accuracy below 12.0 m (0.40 pixels). Moreover, in the quantitative accuracy assessment for the three test sites, the ASPCE method shows the best performance in coastline extraction, achieving a 0.35 pixel-level at the Bohai Sea, China test site. Therefore, the proposed ASPCE method can extract coastline more accurately than can the hard classification methods or other spectral unmixing methods.

Keywords coastline, fully constrained least squares, spatial attraction algorithm, urban development, EO-1 data

1 Introduction

Many megacities (e.g., Shanghai) are located in coastal areas. Although these areas occupy less than 15% of the earth's land surfaces they are home to more than 60% of the world's population (Delhez and Barth, 2011). Moreover, rapid development within the coastal zones has induced an increasing number of ecological and environmental problems that seriously affect urban management (Li et al., 1998, 2003). Therefore, for urban security and sustainable development, it is critical to be able to extract and monitor shorelines quickly (Alonzo et al., 2014; Zhou et al., 2014; Su, 2017). Shorelines are unique terrain features on the earth's surface; shoreline is among the 27 most important features recognized by the IGDC (International Geographic Data Committee) and shorelines

---

Received September 9, 2017; accepted January 15, 2018

E-mails: zhhong@shou.edu.cn (Zhonghua HONG), ylhan@shou.edu.cn (Yanling HAN)

constitute critical information in a Coastal Geographic Information System (CGIS) (Mujabar and Chandrasekar, 2013). A shoreline is defined as an intersection between coastal land and a seawater surface that experiences seawater edge movements as the tides rise and fall (Bird, 1985; Di et al., 2003). The location of the shoreline and its changing boundary over time is fundamental to safe navigation, urban expansion, and coastal resource planning and management. The proxy for shoreline location, or shoreline indicator, generally used in remote sensing imagery is the coastline, which is the boundary between seawater and land at the instant of satellite observation (Gens, 2010; Rahman et al., 2011; Murray et al., 2014).

Remote sensing plays an important role in coastline extraction; consequently, a variety of remote sensing data sources such as SAR images, LiDAR, and multispectral/hyperspectral images are available for use in coastline detection (Boak and Turner, 2005; Bouchahma and Yan, 2014). Coastline extraction from SAR images is a fast-growing field due to SAR's wide spatial coverage, high resolution, and all-day/all-weather imaging capabilities; however, speckle noise and non-uniform sea surface characteristics cause current coastline extraction methods to have low accuracy (Lee and Jurkevich, 1990; Nunziata et al., 2014). LiDAR data can cover hundreds of kilometres of coast in a relatively short period of time, but coastline extracted using these data sources is generally limited in its temporal and spatial availability because of high cost, which negatively affects coastline extraction (Boak and Turner, 2005). Although multispectral images cover large areas and have high temporal frequency, during coastline extraction they generate a discrete signal in only a limited number of broadband spectra that contain less spatial information (Feng et al., 2015; Yang et al., 2015; Pekel et al., 2016). This makes distinguishing seawater and other coastal objects (e.g., vegetation, impervious surfaces, and soil) difficult; thus only low accuracy can be achieved during coastline extraction. In contrast with the other remote sensing image types, hyperspectral images contain nearly continuous spectral information and abundant spatial information, giving them a huge potential for distinguishing seawater from other coastal objects; thus, hyperspectral images can greatly improve the accuracy of coastline extraction.

Various coastline extraction algorithms have been developed for multispectral/hyperspectral images, and these algorithms can be divided into two basic types: hard classification methods and soft classification methods. In hard classification methods, each pixel in the image is allocated to the class with which it has the greatest spectral similarity; however, this allocation method constrains the prediction of water boundaries. Several algorithms have been developed to extract the coastline based on hard classification methods, including density slice analysis (Frazier and Page, 2000; Pajak and Leatherman, 2002), the Support Vector Machine (SVM) (Güneralp et al., 2013), Canny edge detection (Liu and Jezek, 2004), and spectral water indexes (Ryu et al., 2002; Feyisa et al., 2014; Xie et al., 2016a). However, all these hard classification methods can extract coastline only at the pixel-level, which may be insufficient to meet the precise requirements of practical applications in coastal areas with a mixed class composition. In contrast, the soft classification techniques, especially spectral mixture analysis (Foody et al., 2003) can solve the problem of mixed pixels to some extent. Soft classification methods allow a pixel to have both multiple and partial class memberships; thus, they can yield an accurate and realistic representation of seawater, vegetation, impervious surfaces, and soil. Therefore, soft classification techniques can achieve higher accuracy for coastline extraction than can hard classification techniques (Wang, 1990; Foody, 1996).

Spectral mixture analysis that achieves sub-pixel-level accuracy is available for extracting water endmembers of mixed pixels for lakes and urban rivers. Franke et al. (2009) used the Multiple Endmember Spectral Mixture Analysis (MESMA) to extract urban rivers using HyMap data; their experimental results showed that MESMA achieved better results. However, selecting endmembers and determining the endmember types corresponding to spectral signatures using this method is both complex and time consuming. Sankey and Glenn (2011) adopted three different spectral unmixing techniques, including Mixture Tune Matched Filtering (MTMF), Constrained Energy Minimization (CEM), and Linear Spectral Unmixing (LSU), to map water and other objects from Landsat-5 TM and LiDAR data. Among these, the MTMF technique achieved a better performance than did CEM and LSU. However, the MTMF method is applied to linear spectral unmixing using only one constraint condition, namely, the abundance sum-to-one constraint; it does not use the abundance nonnegative constraint condition. Therefore, this method cannot obtain the negative value of the water abundance image, and consequently, it will contain some non-water pixels. Ma et al. (2014) proposed a locally adaptive unmixing method to monitor the water area of Hongjiannao Lake based on MODIS 250 m. Although the problem of the negative value or a water abundance greater than one was resolved as water pixels for pixels with abundance greater than one or land pixels for pixels lower than 0 rather than the abundance nonnegative constraint condition, the extraction of mixed pixels directly affects the final results. Xie et al. (2016b) proposed an automated sub-pixel surface-water mapping method to extract water using Landsat 8 OLI images of urban areas. However, in general, the riverbanks in the Huangpu River area consist mainly of impervious surfaces or are artificial, making it challenging to extract coastline in the Yangtze River Estuary coastal areas containing seawater, vegetation, impervious surfaces, and soil.

Although several sub-pixel-level coastline extraction methods have been proposed in the above studies, existing methods are unsuitable for endmember extraction and type determination in complex coastal zones. Moreover, the aforementioned spectral unmixing methods often used only one constraint condition to estimate water abundance — either the abundance sum-to-one constraint or the abundance nonnegative constraint — which results in worse coastline extraction due to the under- or over-estimation of water abundance in the mixed pixels. In addition, few researchers have applied sub-pixel mapping methods to acquire the specific water position by water abundance, which inevitably affects the accuracy of coastline extraction to some extent. Moreover, these methods were generally applied to coastline extraction for lake and urban river regions; studies for coastal zones are rare, and existing sub-pixel unmixing methods appear to be unsuitable for the more complex coastal zones.

Therefore, in this paper, an automatic sub-pixel coastline extraction method (ASPCE) is proposed. The experimental areas included portions of the South China Sea, the East China Sea, and the Bohai Sea, China and used EO-1 Hyperion data. The objectives were to: (i) develop a technique for coastal mixed-pixel detection and endmember spectrum determination utilizing the W-V-I-S model; (ii) apply a linear unmixing model based on FCLS for estimating seawater endmember abundance; and (iii) obtain the optimal coastline in coastal areas by transforming abundance images into a classification map using the spatial attraction model.

2 Study areas and data sources

2.1 Test sites

The accuracy and feasibility of the ASPCE were tested on three study areas involving different coastal zones: the South China Sea, the East China Sea, and the Bohai Sea, China. These coastal zones included sandy coast, coasts with mud deposition, and rock estuaries. Table 1 summarizes the basic test site characteristics.

2.2 EO-1 hyperion images

As shown in Fig. 1, which is the study areas. For these areas, EO-1 Hyperion data without cloud coverage over the coastal zone were acquired for the experiment and downloaded for free from USGS. The data for the South China Sea was acquired on December 21, 2006; the image covers an area on the upper-left corner and is located at 22°49′58″N, 113°44′34″E, while the lower-right corner is located at 21°53′40″N, 113°36′28″E. The data for the East China Sea was collected on November 8, 2006; the covered area's upper-left corner is 31°37′19″N, 121°34′18″E and its lower-right corner is 30°41′14″N, 121°24′2″E. For the Bohai Sea, China, the data was acquired on November 11, 2006; the image area extends from upper-left (40°20′53″N, 119°41′39″E) to lower-right (39°24′8″N, 119°28′36″E). These data sets belong to the level L1G, a level at which geometric correction, projection registration, and topographic correction have already been made. Moreover, the EO-1 data contains a total of 242 bands with the spectral range of 357–2576 nm and a spatial resolution of 30 m. However, bands 1–7, 58–76, and 225–242 of EO-1 are recorded as bad bands and their value is set to 0 (Barry, 2001); therefore, these bands will not be considered during the subsequent data processing.

2.3 Reference data

The reference data used for the accuracy assessment are described in Table 1. For these three test sites, high spatial resolution images provided by Google Earth$^{\text{TM}}$ were used as reference data. The acquisition dates of the reference data and the EO-1 images were closely matched to minimize the bias in the seawater boundaries that could arise because of large time differences. The dates of acquisition of the EO-1 data and reference data are shown in Table 1.

The "true" boundaries of all the test seawater bodies were digitized manually on-screen from the reference data. In the analysis, the manually digitized coastline was used to assess the accuracy of the different coastline extraction methods when applied to the EO-1 images. Due to the scarcity of high-resolution imagery, some detected water bodies could not be easily validated using Google Earth$^{\text{TM}}$ data. Note that a time span between EO-1 data with Google Earth data is inevitable, and coastline conditions are sometimes extremely variable. To minimize the uncertainty in the coastline reference position, human experience and judgements should be involved in this step to ensure satisfactory validation data.

3 Methodology

Figure 2 shows the entire framework for the coastline extraction process based on the proposed ASPCE method.

Table 1 Details of the three study areas

Study area	Coastal types	Acquisition date of EO-1 data	Acquisition date of reference data
South China Sea	Sandy	December 21, 2006	Google Earth$^{\text{TM}}$ image acquired on January 30, 2007
East China Sea	Mud-deposition	November 8, 2006	Google Earth$^{\text{TM}}$ image acquired on November 12, 2006
Bohai Sea, China	Rock Estuary	November 11, 2006	Google Earth$^{\text{TM}}$ image acquired on December 31, 2006

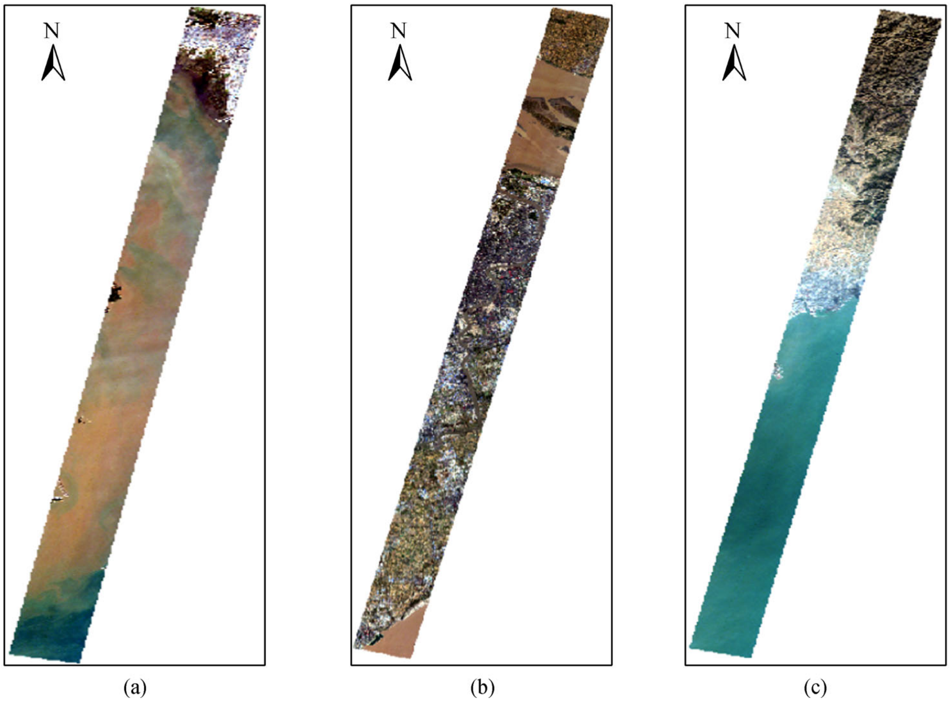

Fig. 1 False-colour composite (RGB: bands 29, 20, 12) EO-1 Hyperion data for the three study areas: (a) South China Sea; (b) East China Sea; and (c) Bohai Sea, China.

The ASPCE approach can be divided into three main steps: 1) detection of coastal mixed pixels and determination of endmember spectrum based on the W-V-I-S model; 2) sub-pixel water abundance estimation of mixed W-V-I-S pixels from the linear spectral unmixing model; and 3) coastline extraction using the spatial attraction model. The methodologies are discussed in detail in the following section.

3.1 Automated mixed W-V-I-S pixel extraction and endmember determination

3.1.1 Calculation of four indexes from the W-V-I-S Model

The surface features for the three test coastal zones contain mainly seawater, vegetation, impervious surfaces, and soil components (Shi and Li, 2010). The surface of each of these coastal components exhibits unique properties and relates to its surrounding site environment, creating a spatially complex ecological system. To understand the dynamics of patterns and process and their interactions in coastal zones, it is necessary to quantify the spatial patterns of the coastal zones and their temporal changes. Therefore, a standard model should be developed to define these coastal component surfaces and to map them in repetitive and consistent ways to be able to accurately extract coastline. Therefore, to obtain the mixed W-V-I-S pixels and the reference spectra of seawater, vegetation, impervious surfaces, and soil corresponding to coastal surface features, the Water-Vegetation-Impervious-Soil (W-V-I-S) model is proposed based on the following four indexes: Normalized Difference Water Index (NDWI), Normalized Difference Vegetation Index (NDVI), Normalized Difference Built-Up Index (NDBI), and Normalized Difference Soil Index (NDSI). This model provides a guideline for decomposing coastal mixed W-V-I-S pixels and links these components to remote sensing spectral characteristics. Moreover, this model, in conjunction with the sub-pixel unmixing method for the EO-1 imagery, functions as an alternative and effective approach for extracting and mapping coastal surface features in coastal zones. The model developed in this study offers a more realistic and robust representation of the true nature of coastlines.

Table 2 summarizes and lists the calculation formulae for the NDWI, NDVI, NDBI, and NDSI, where $\rho(\mathrm{Green})$, $\rho(\mathrm{NIR})$, $\rho(\mathrm{R})$, $\rho(\mathrm{SWIR})$, and $\rho(\mathrm{Yellow})$ denote the reflectance of the respective bands. In this study, based on the wavelength range of the Green, NIR, R, SWIR, and Yellow bands and the reflectance for seawater, vegetation, impervious surfaces, and soil in these bands, the four indexes are calculated using bands 17, 95, 34, 196, and 24 for Green, NIR, R, SWIR, and Yellow, respectively.

3.1.2 Automated mixed W-V-I-S pixel extraction and endmember extraction

To automatically extract mixed W-V-I-S pixels and pure seawater pixels, the valley threshold is used as the starting value when searching for mixed W-V-I-S pixels in the

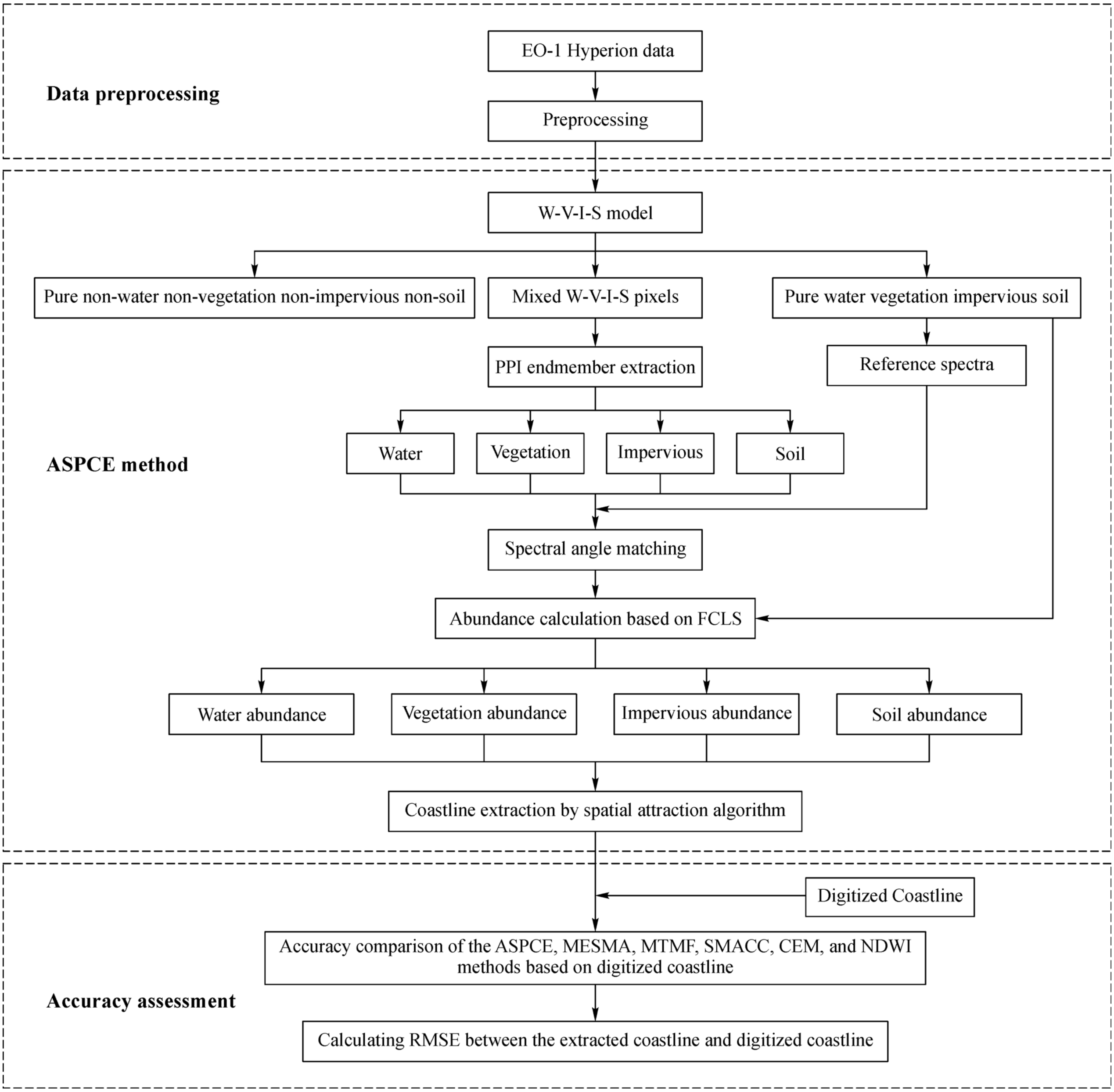

Fig. 2 General framework based on an automatic sub-pixel coastline extraction (ASPCE) method.

Table 2 Calculations for the NDWI, NDVI, NDBI, and NDSI indexes for the extraction of seawater, vegetation, impervious surfaces, and soil, respectively

Four index names	Abbreviation and definition
Normalized Difference Water Index (McFeeters, 1996)	$\mathrm{NDWI}=\left(\rho(\mathrm{Green})-\rho(\mathrm{NIR})\right)/\left(\rho(\mathrm{Green})+\rho(\mathrm{NIR})\right)$
Normalized Difference Vegetation Index (Santos and Negri, 1997)	$\mathrm{NDVI}=\left(\rho(\mathrm{NIR})-\rho(\mathrm{R})\right)/\left(\rho(\mathrm{NIR})+\rho(\mathrm{R})\right)$
Normalized Difference Built-Up Index (Zha et al., 2003)	$\mathrm{NDBI}=\left(\rho(\mathrm{SWIR})-\rho(\mathrm{NIR})\right)/\left(\rho(\mathrm{SWIR})+\rho(\mathrm{NIR})\right)$
Normalized Difference Soil Index (Wolf, 2012)	$\mathrm{NDSI}=\left(\rho(\mathrm{Green})-\rho(\mathrm{Yellow})\right)/\left(\rho(\mathrm{Green})+\rho(\mathrm{Yellow})\right)$

NDWI image histogram between the non-water threshold and the water threshold at the three test sites (see Fig. 3). Locally Weighted Scatter Plot Smoothing (LOWESS) is applied to the original histogram curve. The slope of the histogram curve is used as the discriminant criterion and is usually set to a slope of 30°, 45°, or 60° according to the experimental values (Xie et al., 2016b).

Table 3 shows the corresponding tangential curvatures for pure seawater selection at the three test sites. Mixed pixels are somewhat more easily confused with complex coastal surface features than pure seawater, vegetation, impervious surfaces, and soil pixels. Therefore, for the South China Sea test region, the corresponding tangential curvatures for the non-water threshold and pure water threshold are respectively set to 0.5 and 1.732, namely, 30° and 60°, respectively. For the East China Sea test region, the tangential curvatures range of the mixed W-V-I-S pixels are between 0 and 1.732 on both sides of the starting value; therefore, the non-water threshold and pure water threshold are respectively set to 60° and 60°. For the Bohai Sea test region, the corresponding slopes of 0.5 and 1.732 are selected for the non-water and pure water thresholds. When the curve point of each side first meets the criteria in Table 3, the corresponding abscissa values are selected as the pure seawater threshold.

Table 3 Discriminant criteria for mixed W-V-I-S Pixel Extraction in the South China Sea, East China Sea, and Bohai Sea, China

Test sites	Discriminant criteria
South China Sea	$\lvert\tan\alpha\rvert_{\mathrm{Non-water,left}} \geqslant 0.5, \lvert\tan\alpha\rvert_{\mathrm{water,right}} \geqslant 1.732$
East China Sea	$\lvert\tan\alpha\rvert_{\mathrm{Non-water,left}} \geqslant 1.732, \lvert\tan\alpha\rvert_{\mathrm{water,right}} \geqslant 1.732$
Bohai Sea, China	$\lvert\tan\alpha\rvert_{\mathrm{Non-water,left}} \geqslant 0.5, \lvert\tan\alpha\rvert_{\mathrm{water,right}} \geqslant 1.732$

According to the W-V-I-S model, the various pure seawater, vegetation, impervious surfaces, and soil spectra are selected from the higher NDWI, NDVI, NDBI, and NDSI index values, respectively, which are respectively averaged as the reference spectra.

The methods used to extract pure endmembers of selected seawater, vegetation, impervious surfaces, and soil from W-V-I-S model include the spectral feature space scatterplot from Minimum Noise Fraction (MNF) transform images and the Pixel Purity Index (PPI) algorithm. The PPI is used first to find the most spectrally pure (extreme or unique) pixels in the image data (Harris, 2006);

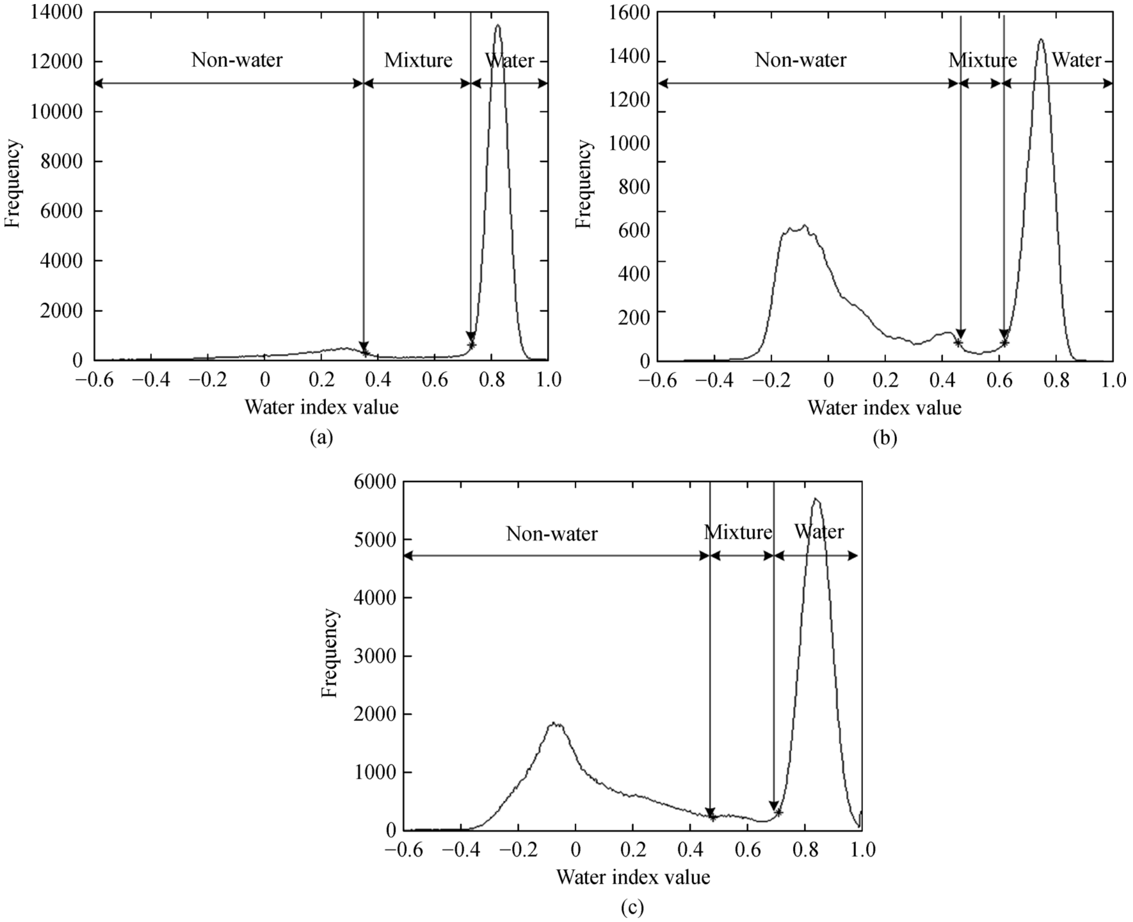

Fig. 3 Histograms of the NDWI in the (a) South China Sea, (b) East China Sea and (c) Bohai Sea, China test sites.

then, the spectral angle method is applied to the spectral matching between endmember spectra and reference spectra based on the W-V-I-S model (Yang et al., 2008).

3.2 Linear spectral unmixing method based on FCLS

The Fully Constrained Least Squares (FCLS) method is used to estimate seawater abundance. Two constraints were imposed: the sum of the endmembers' abundances had to equal one, and the angle of the endmember abundance was limited to between 0 and 1. Moreover, the W-V-I-S model assumes that the surface features in the coastal environment are a linear combination of four components: seawater, vegetation, impervious surfaces, and soil. Therefore, Eq. (1) is the minimum residual error value after iteration when satisfying the two constraints based on coastal surface features, as shown in Eq. (2). Moreover, according to the W-V-I-S model, pure seawater can be effectively obtained because it is contained in large water area in three regions; the reflectance value of pure seawater is determined by calculating an average of the water pixels from the NDWI grey image, and the reflectance values of pure vegetation, impervious surfaces, and soil are determined by calculating the average of selecting several vegetation, impervious surface, and soil spectra from the highest NDVI, NDBI, and NDSI index values, respectively. Then, the seawater abundance can be obtained using Eqs. (1) and (2). The linear unmixing equation can be described as follows (Xie et al., 2016b):

$$\varepsilon = \min\|p_m - (p_w f_w + p_v f_v + p_i f_i + p_s f_s)\|, \quad (1)$$

$$f_w + f_v + f_i + f_s = 1, 0 \leqslant p_w, p_v, p_i, p_s \leqslant 1, \quad (2)$$

where p_w, p_v, p_i, p_w, and p_m are the reflectance values of pure seawater, pure vegetation, pure impervious surfaces, pure soil, and mixed pixels, respectively, and f_w, f_v, f_i, and f_s are the respective abundances of the endmember seawater, vegetation, impervious surfaces, and soil.

3.3 Coastline extraction by the spatial attraction model

Based on the previous seawater abundance results, sub-pixel mapping was first introduced by Atkinson (Atkinson, 1997) to obtain the sub-pixel coastline extraction result. Because coastline is continuous, due to its better spatial correlations, the spatial attraction model was used to obtain the specific positions of endmember seawater, vegetation, impervious surfaces, and soil to improve the accuracy of coastline extraction.

In this research, the scale factor S is determined by the seawater abundance histogram. To facilitate the calculation of distances between sub-pixels and pixels, a Euclidean coordinate system with a vertical X-axis and horizontal Y-axis is defined. This system's origin (0, 0) is at the top left of the sub-pixels (also the top left of the pixels), and the unit distance equals the size of a sub-pixel (Xu et al., 2014). Moreover, to quantify the likelihood of sub-pixels of different classes in the centre of a pixel, Eq. (3) is used to calculate the attraction values for the sub-pixel and its neighbouring pixels, and Eq. (4) is used to define the distances for sub-pixels and pixels as follows:

$$p_{a,b}(c) = Avg\left\{\frac{p_{i,j}(c)}{d(p_{a,b}, p_{i,j})} p_{i,j} \in N_t[p_{a,b}]\right\}, \quad (3)$$

$$(\mathrm{d}p_{a,b}, p_{i,j}) =$$

$$\sqrt{a + 0.5 - S(i + 0.5)^2 + [b + 0.5 - S(j + 0.5)]^2}, \quad (4)$$

where $p_{a,b}(c)$ is the attraction value between sub-pixel $p_{a,b}$ and endmember c; $p_{i,j}(c)$ is the abundance value for the combination of pixel $p_{i,j}$ and endmember c; $N_t[p_{a,b}]$ is the neighbourhood of type t of sub-pixel; and $\mathrm{d}(p_{a,b}, p_{i,j,})$ is the distance between sub-pixel $p_{a,b}$ and pixel $p_{i,j}$ (Mertens et al., 2006).

3.4 Accuracy assessment

The sensitivity of different classifiers to various coastline extraction approaches was evaluated using root mean square error (RMSE) (Li and Gong, 2016) by calculating the distances between the extracted coastline and the digitized coastline for the three test sites. When a mixed-edge pixel was classified as water, the water fraction fell outside the true coastline; similarly, in case where mixed pixels were classified as vegetation, impervious surfaces, or soil (non-water), those fractions of the pixels fell inside the true waterline. Coastline distance changes of the extracted coastline from the different methods compared to the digitized coastline were recorded by using the vertical section method, which is called DSAS (Digital Shoreline Analysis System) in the ArcGIS expansion module, which was developed by the United States Geological Survey Board (Thieler et al., 2009). Considering that the spatial resolution of hyperspectral images is 30 m, section spacing of 30 m, 60 m, 90 m, and 120 m were used in the three test regions for extracting coastline with the proposed ASPCE method and the comparative methods.

4 Results

4.1 Coastline extraction based on ASPCE

4.1.1 Automated endmember extraction and determination based on W-V-I-S model

During data pre-processing, the Minimum Noise Fraction (MNF) transform was selected to reduce the dimension of the EO-1 data and extract the major features of the coastal zones. After the MNF transform, the PPI method (which was introduced in Section 3.1.2) was applied to extract pure endmembers from mixed W-V-I-S pixels using the first few principal components. Fig. 4(a)–4(c) shows the endmember spectra resulting from the PPI method at the South China Sea, the East China Sea, and the Bohai Sea, China test regions, respectively. Classes A1–D1 are the extracted endmember spectra of seawater, vegetation, impervious surfaces, and soil, at the South China Sea test region; Classes A2–D2 and E are the extracted endmember spectra of seawater, vegetation, impervious surfaces, soil, and land water, at the East China Sea test region; and Classes A3–D3 are the extracted endmember spectra of seawater, vegetation, impervious surfaces, and soil, at the Bohai Sea, China test region. In this study, the W-V-I-S model was applied to select pure seawater, vegetation, impervious surfaces, and soil spectral curves from four indexes as reference spectra at the different test sites. As is shown in Fig. 4(a)–4(c), the four endmember libraries of seawater, vegetation, impervious surfaces, and soil were built by averaging the spectra of each ground feature. As Fig. 4 shows, the endmember spectra closely match the reference spectra based on the W-V-I-S model.

To further differentiate the endmember spectra types, the spectral angles between endmember spectra and reference spectra were obtained. As shown in Table 4, compared with the reference spectra of seawater, vegetation, impervious surfaces, and soil, the smallest spectral angles for the classes A1–D1 at the South China Sea test site were 0.1142 rad, 0.0364 rad, 0.0508 rad, and 0.0556 rad, respectively. For the East China Sea test site (Table 5), the smallest spectral angles for the classes A2–D2 were 0.0660 rad, 0.0220 rad, 0.0585 rad, and 0.0350 rad, respectively, and for class E the smallest spectral angle was 0.0670 rad. For the Bohai Sea test site (Table 6), the smallest spectral angles for the classes A3–D3 were 0.0795 rad, 0.0541 rad, 0.0939 rad, and 0.0576 rad, respectively. The smaller the spectral angle, the better match the corresponding object type, meaning that the types of the endmembers of classes A1–D1 in the South China Sea, endmembers of classes A2–D2 in the East China Sea, and endmembers of classes A3–D3 in the Bohai Sea corresponded to seawater,

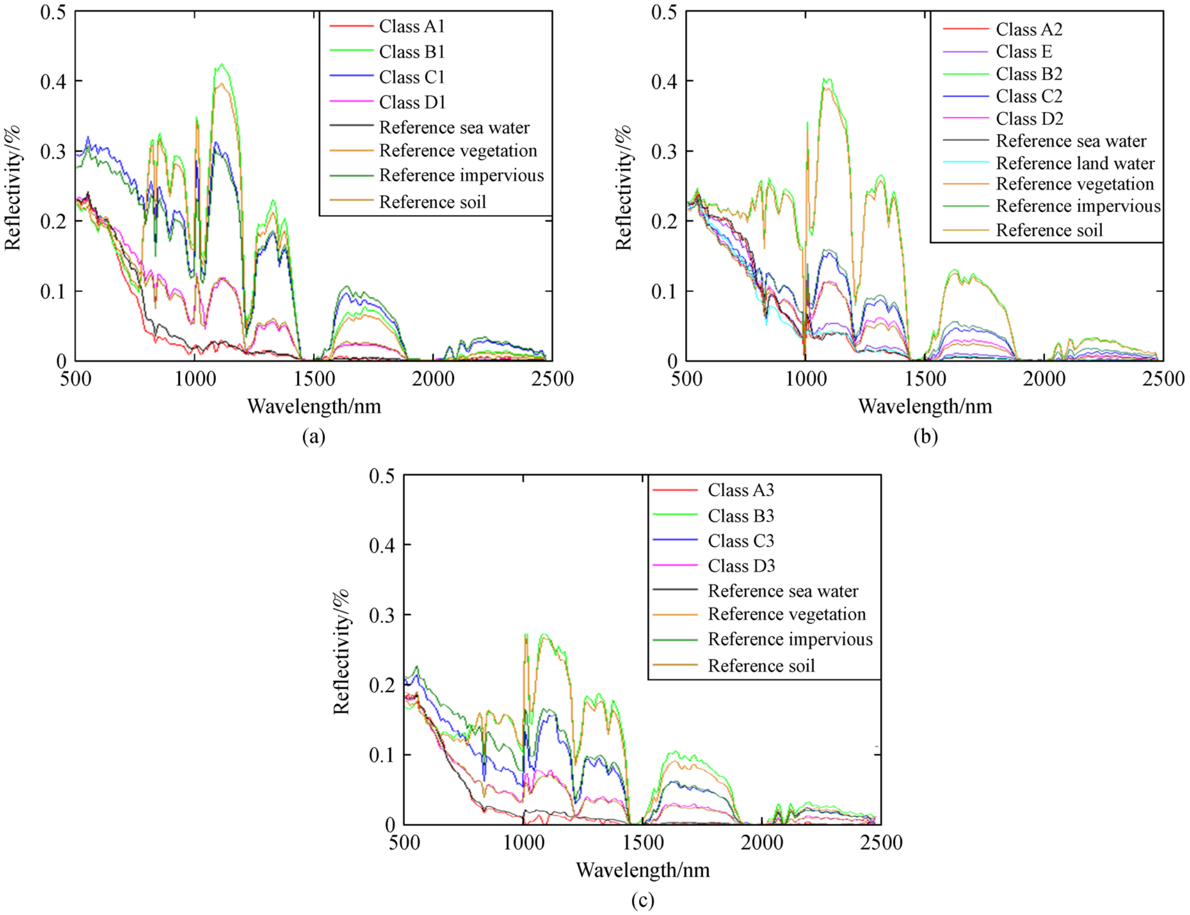

(a)

(b)

(c)

Fig. 4 Extracted spectral curves of ground objects from the PPI algorithm and the reference spectra from four different indexes at (a) South China Sea; (b) East China Sea; and (c) Bohai Sea, China.

Table 4 The angle between the endmember spectrum vector and the reference spectrum vector at the South China Sea test site

Spectrum vector	Spectral angle/rad			
	Class A1	Class B1	Class C1	Class D1
Reference seawater	0.1142	0.9771	0.7160	0.4476
Reference vegetation	0.9768	0.0364	0.3625	0.5821
Reference impervious	0.6563	0.3372	0.0508	0.2678
Reference soil	0.3889	0.5726	0.3161	0.0556

vegetation, impervious surfaces, and soil, respectively. For Class E in the East China Sea, the matching type is land water. As shown in Fig. 4 and Table 5, the ASPCE method clearly distinguished between seawater and land water in the East China Sea test site.

4.1.2 Coastline extraction results based on spatial attraction model

To obtain the optimal spatial distributions of the seawater, vegetation, impervious surfaces, and soil from the abundance images, it was necessary to utilize sub-pixel mapping (introduced in Section 3.3) to acquire more detail from the pixels. The scale factor was determined by the water abundance histogram, because water abundance focuses mainly on abundance values above 0.9; therefore, the scale factor is 3. The experimental results showed that this value accurately locates the optimal position of each endmember.

Complete sub-pixel mapping results with multiple endmembers from the three test regions are shown in Figs. 5–7, respectively. For the South China Sea test region in Fig. 5, the spatial attraction model clearly maps the sandy coast with soil along the coastal zone; this result occurs because the coastal zone at the South China Sea contains a huge range of sand and soil areas due to wave and/or wind accumulation over a long timescale. Figure 6 shows the endmember mapping and coastline extraction results from the East China Sea test region. Because this test region includes the Yangtze River estuary and the Huangpu River, a large quantity of fine sediment has been carried into the sea by the rivers and has been affected by tidal currents and waves for a long time in the Yangtze River estuary. However, when using the ASPCE method, the results are clearly distinct from the seawater and land water in the mixed W-V-I-S pixels. Regarding the Bohai Sea, China test region in Fig. 7, compared with the original image, the endmember image clearly shows the specific classifications of the extracted coastal endmembers. Specifically, this coastal boundary consists of impervious endmember surfaces due to geological structures or an artificial coast. These experimental results show that the ASPCE method achieves better endmember mapping and coastline extraction results.

4.2 Compared methods and accuracy assessment

To compare the accuracy of the proposed ASPCE method with other methods, four widely used mixture pixel

Table 5 The angle between the endmember spectrum vector and the reference spectrum vector at the East China Sea test site

Spectrum vector	Spectral angle/rad				
	Class A2	Class E	Class B2	Class C2	Class D2
Reference seawater	0.0660	0.0789	0.8104	0.4422	0.3288
Reference land water	0.0962	0.0670	0.8018	0.4245	0.3031
Reference vegetation	0.8027	0.7477	0.0220	0.3754	0.4995
Reference impervious	0.4811	0.4263	0.3528	0.0585	0.1663
Reference soil	0.3110	0.2584	0.5236	0.1465	0.0350

Table 6 The angle between the endmember spectrum vector and the reference spectrum vector at the Bohai Sea, China test site

Spectrum vector	Spectral angle/rad			
	Class A3	Class B3	Class C3	Class D3
Reference seawater	0.0795	1.0095	0.6876	0.4058
Reference vegetation	0.9667	0.0541	0.3654	0.6331
Reference impervious	0.6011	0.3744	0.0939	0.2685
Reference soil	0.3870	0.5810	0.2699	0.0576

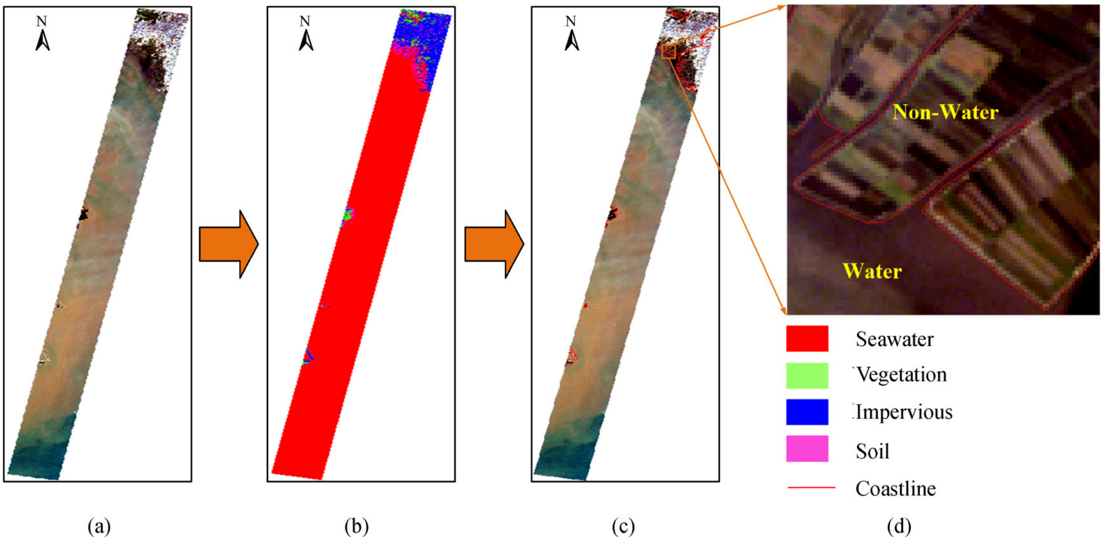

Fig. 5 Coastline extraction results based on the ASPCE method at the South China Sea test site. (a) Original image; (b) sub-pixel mapping result with each different endmember; (c) coastline extraction based on ASPCE method; (d) partial magnification of (c).

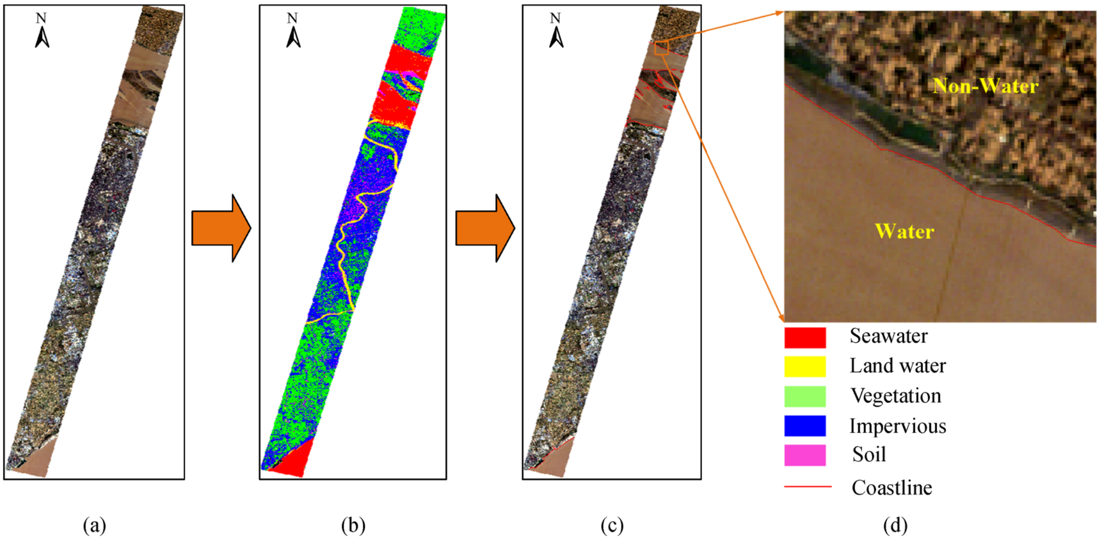

Fig. 6 Coastline extraction results based on the ASPCE method at the East China Sea test site. (a) Original image; (b) sub-pixel mapping result with each different endmember; (c) coastline extraction based on ASPCE method; (d) partial magnification of (c).

unmixing methods, the Multiple Endmember Spectral Mixture Analysis (MESMA), Mixture Tuned Matched Filtering (MTMF), Sequential Maximum Angle Convex Cone (SMACC), and Constrained Energy Minimization (CEM), and one classical Normalized Difference Water Index (NDWI) were selected to perform coastline extraction comparisons with the proposed method.

4.2.1 Coastline extraction results from different methods

The images in the first column of Figs. 8(a), 8(h), and 8(o) show the digitized coastlines. The images in the second column of Figs. 8(b), 8(i), and 8(p) show the coastline extraction results of the ASPCE method for the different study areas. The third through the seventh columns of Fig. 8 show the coastlines extracted by the compared methods. From a visual inspection, it can be seen that with the extracted coastlines of the SMACC, CEM, and NDWI methods in the South China Sea (Figs. 8(e), 8(f), and 8(g)), in the East China Sea (Figs. 8(l), 8(m), and 8(n)), and at the Bohai Sea, China (Figs. 8(s), 8(t), and 8(u)), deviations from the digitized coastline are more serious. Moreover, Figure 9 clearly shows that those methods obtained the worst results compared with the proposed method. The MESMA and MTMF methods (Figs. 8(c), 8(d)) in the South China Sea, (Figs. 8(j) and 8(k)) in the East China

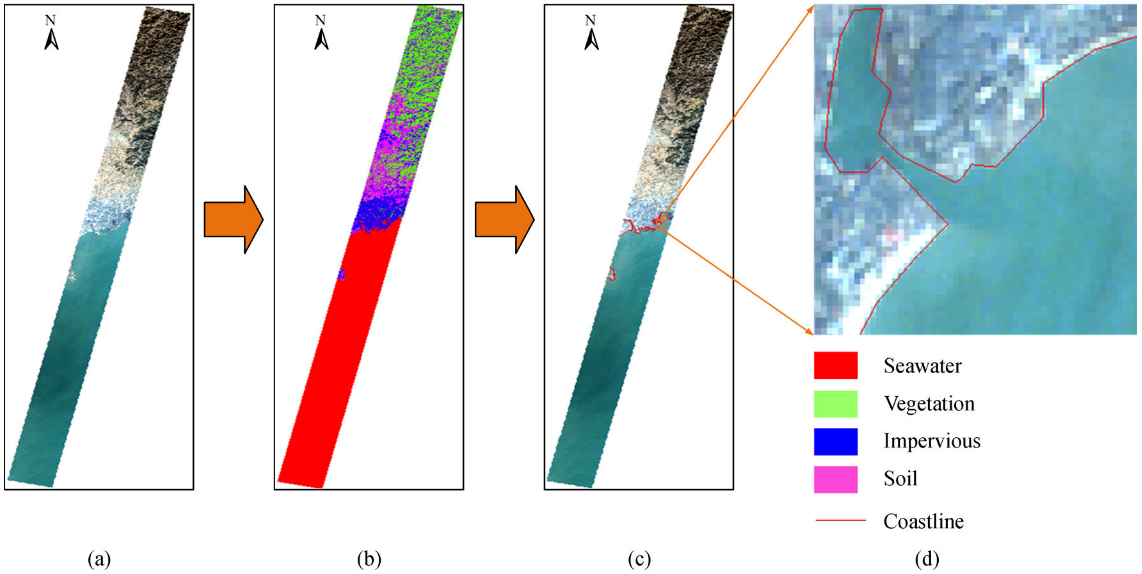

Fig. 7 Coastline extraction results based on the ASPCE method at the Bohai Sea, China test site. (a) Original image; (b) sub-pixel mapping result with each different endmember; (c) coastline extraction based on ASPCE method; (d) partial magnification of (c).

Sea, and (Figs. 8(q) and 8(r)) in the Bohai Sea, China obtained better results than the other three methods; however, the detail regions demonstrate that they included more errors than do the results of the proposed ASPCE method in Fig. 9. ASPCE achieves the best visual accuracy in all the sub-pixels. For the complex coastal zones, especially the East China Sea test region in Fig. 9(b), the ASPCE method is the most sensitive to water body information; it can accurately extract water bodies from mixed pixels and avoid omission and misclassification errors. Moreover, the proposed ASPCE method better acquires the specific locations of the sub-pixels inside a pixel than do the other comparison methods. These results show the coastline extraction results of the proposed ASPCE method provide considerably better coastline locations than do the compared methods.

More specifically, Figure 9 shows that the coastline extraction derived from the ASPCE method has the highest consistency with the digitized coastline in each test site. For the South China Sea test site in Fig. 9(a), the ASPCE method shows a better coastline extraction result than do the compared methods, especially NDWI, which obtains the worst result. For the East China Sea test site containing a large amount of sediment in Fig. 9(b)—especially in the Yangtze River estuary region—the proposed method is consistently better at suppressing sediment and other non-water surfaces, enhancing water absorption, and obtaining the best coastline extraction. In contrast, the compared methods extract worse results because of insufficient information, and they omit the small water bodies. For the Bohai Sea, China test site in Fig. 9(c), the coastal area is rocky and includes no non-water surfaces other than rocks. Therefore, all the methods achieve better coastline extraction results. However, the coastline extracted using the ASPCE method has the highest consistency with the digitized coastline. A visual inspection of the detail area clearly shows that the ASPCE method efficiently extracts coastline from different coastal zones.

4.2.2 Accuracy analysis

The RMSE method introduced in Section 3.4 was used to analyse the accuracy of the various methods. Figure 10 shows the accuracy of RMSE based on the ASPCE, MESMA, MTMF, SMACC, CEM, and NDWI methods in the different study areas. The experimental results clearly show that the proposed ASPCE method significantly outperforms the other comparison methods when the section spacing is 30 m, 60 m, 90 m, or 120 m.

As shown in Fig. 10, the proposed ASPCE, MESMA, MTMF, SMACC, CEM, and NDWI methods are consistent with the RMSE in terms of the different section spacing in the three study areas. That is, the accuracy of the extracted coastline becomes worse as the spacing increases. Compared with the digitized coastline, a smaller spacing more clearly expresses the extracted coastline results by the different methods. Moreover, considering the use of images with a resolution of 30 m/pixel in this study, using the 30 m section spacing obtains a more accurate coastline extraction than does using other section spacing values.

For the 30 m section spacing, the quantitative sub-pixel accuracy assessment results are summarized in Fig. 11. The RMSE values of the proposed ASPCE method for the extracted coastline are 10.5 m, 11.9 m, and 12.0 m at the Bohai Sea, China, South China Sea, and East China Sea, respectively—that is, 0.35 pixels, 0.38 pixels, and 0.40 pixels, respectively. When compared to the MESMA,

Fig. 8 Comparison of the coastline extraction results. First row, (a)–(g) are, respectively, the digital coastline and coastline extractions from the proposed method and the compared methods (MESMA, MTMF, SMACC, CEM, and NDWI) in the South China Sea; Second row, (h)–(n) are, respectively, the digital coastline and coastline extractions from the proposed method and the compared methods (MESMA, MTMF, SMACC, CEM, and NDWI) in the East China Sea; Third row, (o)–(u) are, respectively, the digital coastline and coastline extractions from the proposed method and the compared methods (MESMA, MTMF, SMACC, CEM, and NDWI) in the Bohai Sea, China.

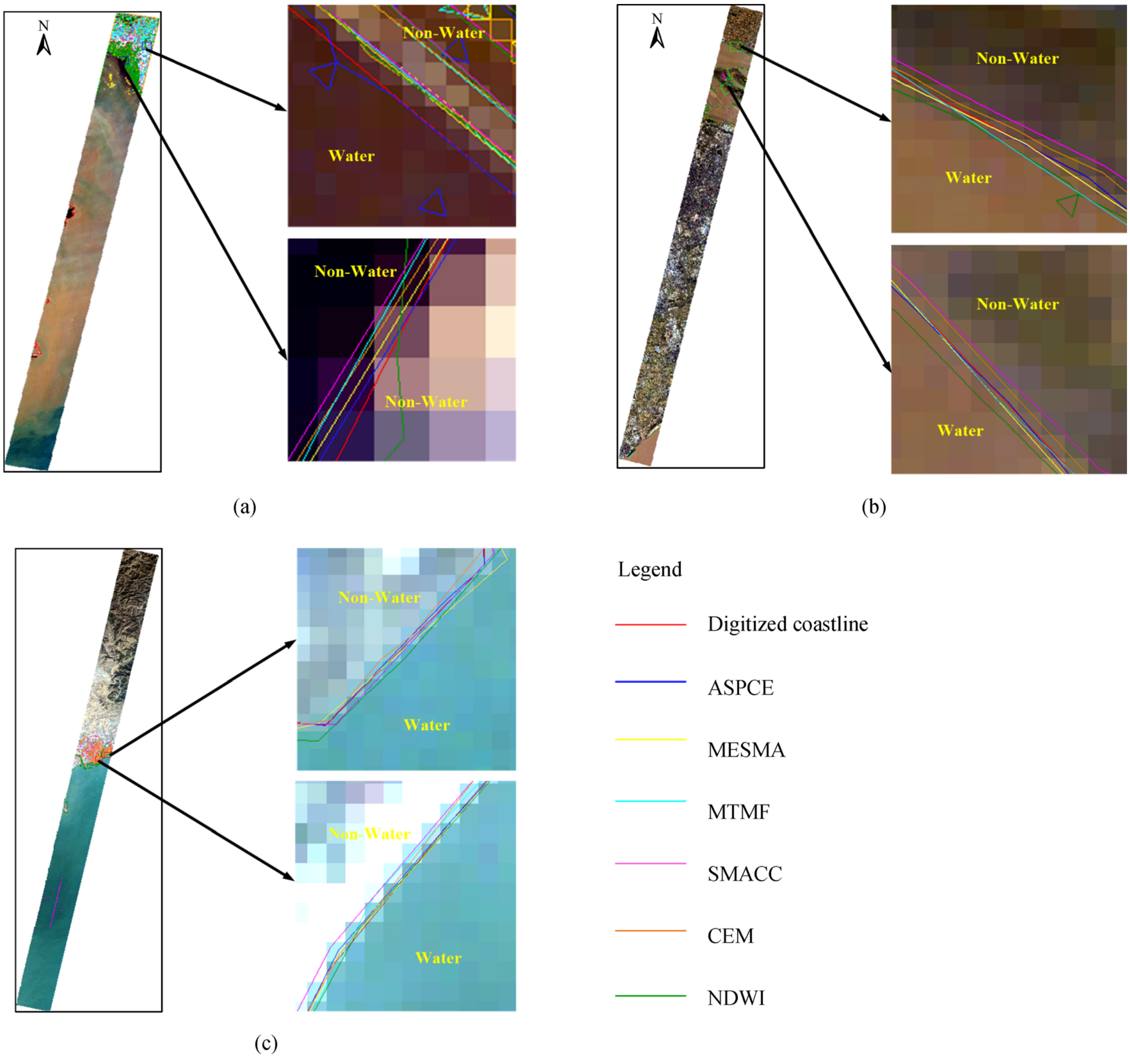

(a)

(b)

(c)

Fig. 9 Detail results of the coastline extracted by seven methods overlaid on the original image at the (a) South China Sea, (b) East China Sea, and (c) Bohai Sea, China, respectively.

MTMF, SMACC, CEM, and NDWI method results in the three test regions, for the Bohai Sea, China test region, the ASPCE method improves the accuracy by 24.5%, 39.6%, 44.7%, 47.5%, and 52.3%, respectively. For the South China Sea test region, the ASPCE method improves the accuracy by 15% over MESMA, 33.5% over MTMF, 40.5% over SMACC, 47.3% over CEM, and 48.3% over NDWI. For the East China Sea test region, the ASPCE method improves the accuracy by 18.4%, 29.4%, 36.8%, 41.5%, and 48.7%, respectively over the MESMA, MTMF, SMACC, CEM, and NDWI methods. The comparatively high accuracy achieved by ASPCE is attributable to the fact that surface features in coastal zones are complex, especially in the East China Sea test region, and it is difficult to obtain a satisfactory result using the MESMA, MTMF, SMACC, CEM, and NDWI methods. The ASPCE yields a better performance by accurately extracting the mixed W-V-I-S pixels and determining the endmember spectra based on the W-V-I-S model in complex coastal zones. In addition, the strategy used to determine the sub-pixel distribution in the ASPCE method reduces the influence of inaccurate fraction images caused by the spectral unmixing algorithm, while the other comparison methods introduce more errors, due to both insufficient information and the inaccurate results of the spectral unmixing. The proposed method determines more details from mixed pixels. Based on the statistical results, the proposed ASPCE method exhibits higher sub-pixel mapping accuracy than do the pixel-level methods CEM and NDWI or the sub-pixel-level methods MESMA, MTMF, and SMACC.

This result occurs because the CEM method considers the considerable amount of shade that exists in coastal zones. The spectral characteristics of shade and water surfaces are similar in some cases; therefore, it is difficult for the CEM method to clearly distinguish between water

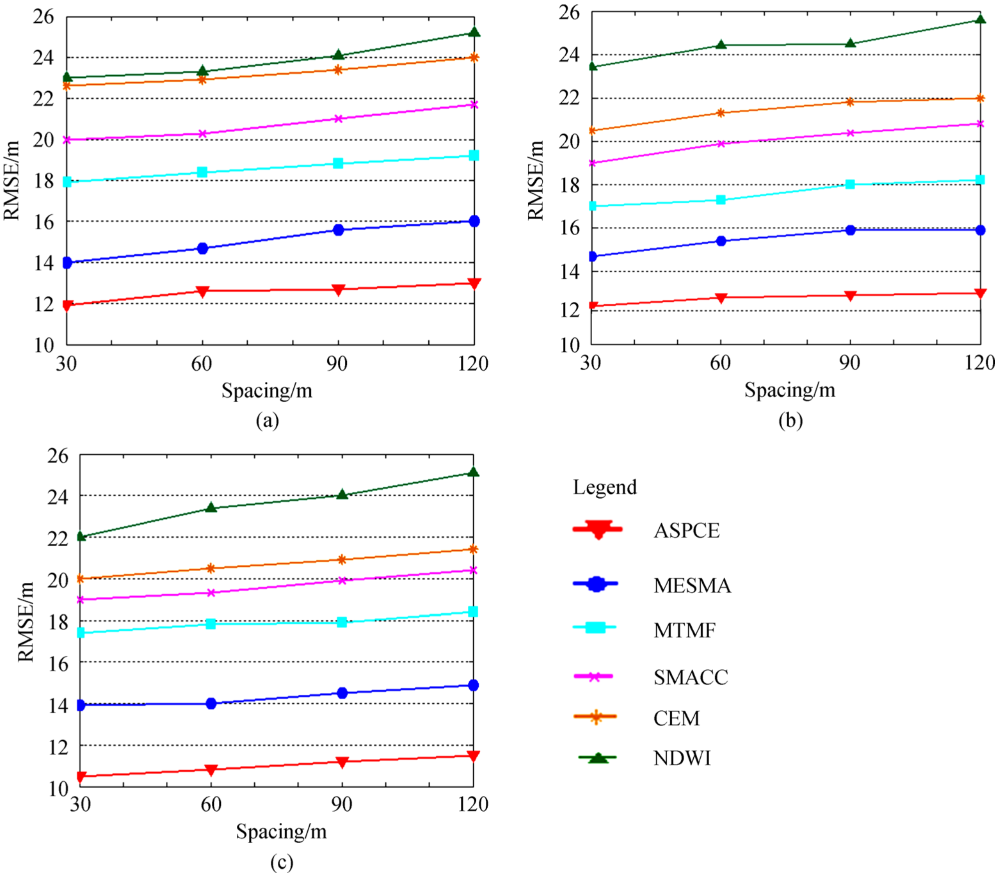

(a)

(b)

(c)

Fig. 10 RMSE value of extracted coastlines with the proposed ASPCE, MESMA, MTMF, SMACC, CEM, and NDWI methods using different section spacing at the (a) South China Sea test site; (b) East China Sea test site; (c) Bohai Sea, China test site.

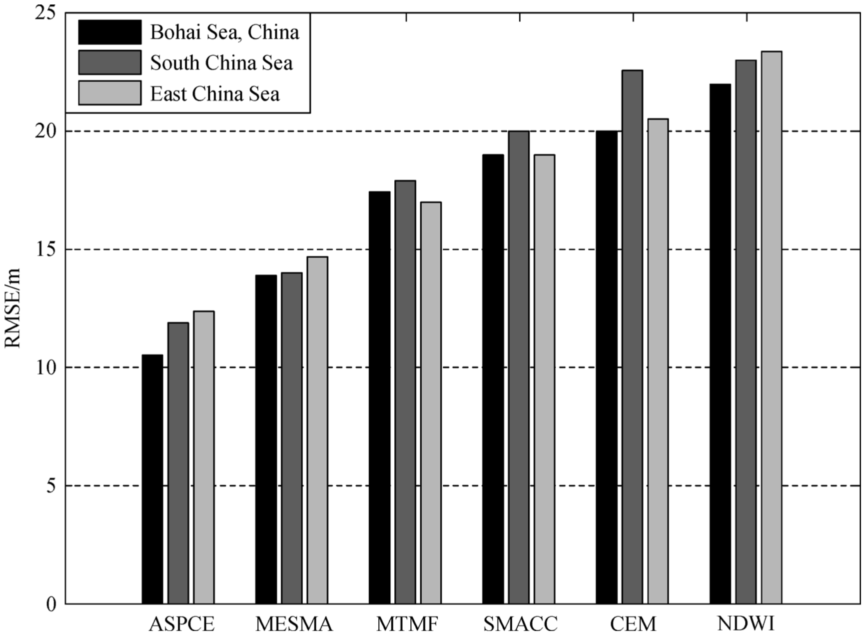

Fig. 11 RMSE values of extracted coastlines by the different methods at 30 m section spacing in the Bohai Sea, China, East China Sea, and South China Sea sites.

and shade. In addition, the hard-classification NDWI method allocates each pixel in the image to the class with which it has the greatest spectral similarity, which constrains the prediction of water boundaries. Moreover, the optimal threshold value of NDWI is generally difficult to determine. Therefore, compared with the proposed ASPCE method, these methods yield worse coastline extraction results. However, although the extracted coastlines of the MESMA, MTMF, and SMACC methods achieve better performances than do the CEM and NDWI methods, due to insufficient information and errors in spectral unmixing, the MTMF and SMACC methods do not strictly satisfy the abundance constraints; thus, they obtain worse coastline extraction results than the MESMA method. Among the compared methods, MESMA achieves the best coastline extraction accuracy; however, the combination of endmembers is more complex in these experimental study areas, and the large number of pixels makes MESMA time consuming, which is not conducive to mixed-pixel unmixing over large areas.

A close look at the RMSE accuracy for each test site reveals that the coastline extraction derived from the proposed method has the highest consistency with the digital coastline and shows that ASPCE method has the ability to achieve an RMSE accuracy of better than 12.0 m (0.40 pixels). However, the coastline extraction of ASPCE is least accurate in the East China Sea test site. This is because the East China Sea site includes the Yangtze River estuary coastal zone, in which large amounts of fine sediment have been carried by rivers into the sea over a long time, forming a mud-deposition coastal zone, and seawater containing the suspended sediment has an impact on the water spectrum extracted using the ASPCE method. Among the other test sites, the Bohai Sea, China site features a rock estuary coastal zone, and the South China Sea site has a sandy coastal zone; thus, the ASPCE method obtains higher coastline extraction accuracy due to the purity of the seawater in these areas. Note that the minimum temperature is approximately 0 degrees according to the weather in Bohai on November 11, 2006; therefore, temperature did not affect the coastline extraction because these data were obtained in daytime and no sea ice was present in this test region.

The water areas are divided into seawater and land water in the East China Sea test site because this study region contains large land water areas of the Huangpu River. However, the endmember spectral characteristics of land water can be clearly distinguished from Yangtze River estuary seawater because of the fine sediment; therefore, the seawater endmember spectrum was used to extract coastline in this study area. However, the South China Sea and Bohai Sea, China test sites contain almost pure seawater, and the endmember spectral characteristics of land water and seawater are similar for these study regions; therefore, the endmember spectra of land water and seawater were combined into one endmember spectrum to extract coastline.

Therefore, based on the statistical accuracy results of ASPCE compared with the MESMA, MTMF, SMACC, CEM, and NDWI methods, the coastline extraction effect of the proposed ASPCE method suggests that it can extract coastline at sub-pixel-level accuracy.

4.2.3 Error analysis

The ASPCE method achieved the highest coastline extraction accuracy compared with the related methods; however, some errors still exist in the final extracted coastline. Through a comprehensive analysis of the error statistics, we confirmed that the error sources stem from the following three aspects: 1) all three test images were acquired in coastal zones with complex ground surface conditions, especially in the East China Sea site, which includes many ships and small stones at coastal edges that can easily be confused with seawater due to high spectral feature similarities (Xie et al., 2014); 2) the linear spectral unmixing model was applied for endmember abundance estimation in this study; however, in reality, the measured signal of the sensor always includes the interactions of electromagnetic radiation with the multiple constituents within each pixel (Keshava and Mustard, 2002); thus, not all objects are linear in the experimental images, and consequently, it is inaccurate to regard all pixels as linear models; and 3) a substantial timespan between the acquired EO-1 data and the Google Earth data is inevitable; coastline conditions are sometimes extremely varied, and these differences can affect the measurement of coastline extraction accuracy.

5 Conclusions

To ensure urban security and sustainable development in the coastal zones, coastline information should be extracted accurately and should not be limited to the pixel level. In this paper, an automated sub-pixel coastline extraction method is proposed for three experimental areas: the South China Sea, the East China Sea, and the Bohai Sea, China. The main results of this study show that the proposed ASPCE method is more effective for extracting coastlines.

1) First, the W-V-I-S model based on four indexes was applied to coastline extraction from EO-1 data in the different test regions; this approach contributes to improving the detection accuracy of mixed W-V-I-S pixels, endmember spectra determination, and computational efficiency.

2) Utilizing the FCLS method simultaneously satisfies two constraint conditions, namely, that the sum of the endmembers' abundances should be equal to one, and that

the angle of endmember abundance should be limited to between 0 and 1. This method efficiently improves the unmixing accuracy from mixed W-V-I-S pixels and provides accurate seawater abundance for use with the spatial attraction model, which obtains the specific sub-pixel locations and extracts coastline accurately in different coastal zones.

3) The experimental results indicate that the ASPCE, MESMA, MTMF, SMACC, CEM, and NDWI methods exhibit consistency across the 30 m, 60 m, 90 m, and 120 m section spacing — that is, the accuracy of the extracted coastline degrades as the spacing increases.

4) Using 30 m section spacing, the accuracy of the extracted coastline based on proposed ASPCE method is 0.39 pixels, 0.40 pixels, and 0.35 pixels in the South China Sea, East China Sea, and Bohai Sea, China test regions, respectively, and the ASPCE method significantly outperforms the compared methods. The results from each test region revealed that the coastline extraction using the proposed method had the highest consistency with the digital coastline, showing that the ASPCE method has the ability to achieve an accuracy of better than 12.0 m (0.40 pixels). Moreover, the coastline extraction accuracy of the ASPCE method was best in the Bohai Sea, China site due to its rocky coast and lack of complex surface features, while its coastline extraction result was the worst in the East China Sea site due to the complex coastal surface features.

Therefore, the quantitative accuracy results indicate that the ASPCE method proposed in this paper can accurately extract coastline from the mixed pixels of complex coastal zones and achieve more precise results than can the traditional pixel-level methods based on hard classification or other spectral unmixing methods based on soft classification.

Acknowledgements The work described in this paper was substantially supported by the National Natural Science Foundation of China (Grant Nos. 41401489 and 41376178), Shanghai Foundation for University Youth Scholars (Project No. ZZHY13033), and the Innovation Programme of the Shanghai Municipal Education Commission (Project No. 15ZZ082).

References

Alonzo M, Bookhagen B, Roberts D A (2014). Urban tree species mapping using hyperspectral and lidar data fusion. Remote Sens Environ, 148(148): 70–83

Atkinson P M (1997). Mapping Sub-Pixel Boundaries from Remotely Sensed Images. In: Kemp Z, ed. Innovations in GIS 4. London: Taylor and Francis: 166–180

Barry P (2001). EO-1 Hyperion Science Data User's Guide, Level 1_B. TRW Space. Defense and Information Systems, 555–557

Bird E C F (1985). Coastline Changes. A global review. New York: John Wiley and Sons Inc.,108

Boak E H, Turner I L (2005). Shoreline definition and detection: a review. J Coast Res, 21(4): 688–703

Bouchahma M, Yan W (2014). Monitoring shoreline change on Djerba Island using GIS and multi-temporal satellite data. Arab J Geosci, 7 (9): 3705–3713

Delhez E J M, Barth A (2011). Science based management of coastal waters. J Mar Syst, 88(1): 1–2

Di K, Wang J, Ma R, Li R (2003). Automatic shoreline extraction from high resolution IKONOS satellite imagery. Cortex, 49(1): 184–199

Feng Y, Liu Y, Liu D (2015). Shoreline mapping with cellular automata and the shoreline progradation analysis in Shanghai, China from 1979 to 2008. Arab J Geosci, 8(7): 4337–4351

Feyisa G L, Meilby H, Fensholt R, Proud S R (2014). Automated water extraction index: a new technique for surface water mapping using Landsat imagery. Remote Sens Environ, 140(1): 23–35

Foody G M (1996). Approaches for the production and evaluation of fuzzy land cover classifications from remotely-sensed data. Int J Remote Sens, 17(7): 1317–1340

Foody G M, Muslim A M, Atkinson P M (2003). Super-resolution Mapping of the Shoreline through Soft Classification Analyses. IEEE International Geoscience and Remote Sensing Symposium, (6): 3429–3431

Franke J, Roberts D A, Halligan K, Menz G (2009). Hierarchical multiple endmember spectral mixture analysis (MESMA) of hyperspectral imagery for urban environments. Remote Sens Environ, 113(8): 1712–1723

Frazier P S, Page K J (2000). Water body detection and delineation with Landsat TM data. Photogramm Eng Remote Sensing, 66(12): 1461–1468

Gens R (2010). Remote sensing of coastlines: detection, extraction and monitoring. Int J Remote Sens, 31(7): 1819–1836

Güneralp İ, Filippi A M, Hales B U (2013). River-flow boundary delineation from digital aerial photography and ancillary images using Support Vector Machines. GIsci Remote Sens, 50(1): 1–25

Harris A T (2006). Spectral mapping tools from the earth sciences applied to spectral microscopy data. Cytometry A, 69A(8): 872–879

Keshava N, Mustard J F (2002). Spectral unmixing. IEEE Signal Process Mag, 19(1): 44–57

Lee J S, Jurkevich I (1990). Coastline detection and tracing In SAR images. IEEE Trans Geosci Remote Sens, 28(4): 662–668

Li R, Di K, Ma R (2003). 3-D shoreline extraction from IKONOS satellite imagery. Mar Geod, 26(1–2): 107–115

Li R, Keong C W, Ramcharan E, Kjerfve E, Willis D (1998). A coastal GIS for shoreline monitoring and management-case study in Malaysia. Surveying and Land Information Systems, 58(3): 157–166

Li W, Gong P (2016). Continuous monitoring of coastline dynamics in western Florida with a 30-year time series of Landsat imagery. Remote Sens Environ, 179: 196–209

Liu H, Jezek K C (2004). Automated extraction of coastline from satellite imagery by integrating Canny edge detection and locally adaptive thresholding methods. Int J Remote Sens, 25(5): 937–958

Ma B, Wu L, Zhang X, Li X, Liu Y, Wang S (2014). Locally adaptive unmixing method for lake-water area extraction based on MODIS 250 m bands. Int J Appl Earth Obs Geoinf, 33(1): 109–118

McFeeters S K (1996). The use of the normalized difference water index (NDWI) in the delineation of open water features. Int J Remote Sens, 17(7): 1425–1432

Mertens K C, De Baets B, Verbeke L P C, De Wulf R R (2006). A sub-pixel mapping algorithm based on sub-pixel/pixel spatial attraction models. Int J Remote Sens, 27(15): 3293–3310

Mujabar P S, Chandrasekar N (2013). Shoreline change analysis along the coast between Kanyakumari and Tuticorin of India using remote sensing and GIS. Arab J Geosci, 6(3): 647–664

Murray N J, Clemens R S, Phinn S R, Possingham H P, Fuller R A (2014). Tracking the rapid loss of tidal wetlands in the Yellow Sea. Front Ecol Environ, 12(5): 267–272

Nunziata F, Migliaccio M, Li X, Ding X (2014). Coastline extraction using dual-polarimetric COSMO-SkyMed PingPong Mode SAR Data. IEEE Geosci Remote Sens Lett, 11(1): 104–108

Pajak M J, Leatherman S (2002). The high water line as shoreline indicator. J Coast Res, 18(2): 329–337

Pekel J F, Cottam A, Gorelick N, Belward A S (2016). High-resolution mapping of global surface water and its long-term changes. Nature, 540(7633): 418–422

Rahman A F, Dragoni D, El-Masri B (2011). Response of the Sundarbans coastline to sea level rise and decreased sediment flow: a remote sensing assessment. Remote Sens Environ, 115(12): 3121–3128

Ryu J H, Won J S, Min K D (2002). Waterline extraction from Landsat TM data in a tidal flat: a case study in Gomso Bay, Korea. Remote Sens Environ, 83(3): 442–456

Sankey T, Glenn N (2011). Landsat-5 TM and Lidar fusion for sub-pixel juniper tree cover estimates in a western rangeland. Photogramm Eng Remote Sensing, 77(12): 1241–1248

Santos P, Negri A J (1997). A comparison of the normalized difference vegetation index and rainfall for the Amazon and northeastern Brazil. J Appl Meteorol, 36(7): 958–965

Shi Y F, Li X C (2010). Land use dynamic evolution simulation of the north branch of Yangtze River Estuary based on SLEUTH model. Modern Surveying & Mapping, 3: 003 (in Chinese)

Su W Z (2017). Measuring the past 20 years of urban-rural land growth in flood-prone areas in the developed Taihu Lake watershed, China. Front Earth Sci, 11(2): 361–371

Thieler E R, Himmelstoss E A, Zichichi J L, Ergul A (2009). The Digital Shoreline Analysis System (DSAS) version 4.0-An ArcGIS Extension for Calculating Shoreline Change. US Geological Survey

Wang F (1990). Fuzzy supervised classification of remote sensing images. IEEE Trans Geosci Remote Sens, 28(2): 194–201

Wolf A F (2012). Using Worldview-2 Vis-NIR multispectral imagery to support land mapping and feature extraction using normalized difference index ratios SPIE Defense, Security, and Sensing. International Society for Optics and Photonics, Vol 8390

Xie H, Luo X, Xu X, Pan H, Tong X (2016 a). Evaluation of Landsat 8 OLI imagery for unsupervised inland water extraction. Int J Remote Sens, 37(8): 1826–1844

Xie H, Luo X, Xu X, Pan H, Tong X (2016 b). Automated subpixel surface water mapping from heterogeneous urban environments using Landsat 8 OLI Imagery. Remote Sens, 8(7): 584

Xie H, Luo X, Xu X, Tong X, Jin Y, Pan H, Zhou B X (2014). New hyperspectral difference water index for the extraction of urban water bodies by the use of airborne hyperspectral images. J Appl Remote Sens, 8(1): 085098

Xu X, Zhong Y, Zhang L (2014). A sub-pixel mapping method based on an attraction model for multiple shifted remotely sensed images. Neurocomputing, 134: 79–91

Yang C, Everitt J H, Bradford J M (2008). Yield estimation from hyperspectral imagery using spectral angle mapper (SAM). Trans ASABE, 51(2): 729–737

Yang Y, Liu Y, Zhou M, Zhang S, Zhan W, Sun C, Duan Y (2015). Landsat 8 OLI image based terrestrial water extraction from heterogeneous backgrounds using a reflectance homogenization approach. Remote Sens Environ, 171: 14–32

Zha Y, Gao J, Ni S (2003). Use of normalized difference built-up index in automatically mapping urban areas from TM imagery. Int J Remote Sens, 24(3): 583–594

Zhou D, Zhao S, Liu S, Zhang L, Zhu C (2014). Surface urban heat island in China’s 32 major cities: spatial patterns and drivers. Remote Sens Environ, 152(152): 51–61